Integrated multi-omics reveals anaplerotic insufficiency in methylmalonyl-CoA mutase deficiency

Patrick Forny[1a], Ximena Bonilla[2ab], David Lamparter[3,8ab], Wenguang Shao[4,8ab], Tanja Plessl[1], Caroline Frei[1], Anna Bingisser[1], Sandra Goetze[4,8], Audrey van Drogen[4,8], Keith Harshman[3,8], Patrick G. A. Pedrioli[4,7,8,9], Cedric Howald[3], Martin Poms[10], Florian Traversi[1], Sarah Cherkaoui[1], Raphael J. Morscher[1], Luke Simmons[5], Merima Forny[1], Ioannis Xenarios[6,8], Ruedi Aebersold[7,8], Nicola Zamboni[7,8], Gunnar Raetsch[2], Emmanouil Dermitzakis[3,8], Bernd Wollscheid[4,8,9*], Matthias R. Baumgartner[1*], D. Sean Froese[1*]

[1] Division of Metabolism, University Children's Hospital Zurich and Children's Research Center, University of Zurich, Switzerland

[2] Biomedical Informatics, Department of Computer Science, Swiss Federal Institute of Technology / ETH Zürich, Switzerland

[3] Health 2030 Genome Center, Geneva, Switzerland

[4] Institute of Translational Medicine, Department of Health Science and Technology, Swiss Federal Institute of Technology / ETH Zürich, Switzerland

[5] Division of Child Neurology, University Children's Hospital Zurich, University of Zurich, Switzerland

[6] Agora Center, Rue du Bugnon 21, Lausanne, Switzerland

[7] Institute of Molecular Systems Biology, Department of Biology, Swiss Federal Institute of Technology / ETH Zürich, Switzerland

[8] PHRT Swiss Multi-OMICS Center / smoc.ethz.ch, Switzerland

[9] Swiss Institute of Bioinformatics, Lausanne, Switzerland

[10] Division of Clinical Chemistry, University Children's Hospital Zurich, University of Zurich, Switzerland

[a] These authors contributed equally to this study.

[b] These authors are listed alphabetically.

[*] Correspondence: sean.froese@kispi.uzh.ch (Lead Contact), matthias.baumgartner@kispi.uzh.ch, bernd.wollscheid@hest.ethz.ch

Abstract

Multi-layered omics approaches can help define relationships between genetic factors, biochemical processes and phenotypes thus extending research of inherited diseases beyond identifying their monogenic cause [1]. We implemented a multi-layered omics approach for the inherited metabolic disorder methylmalonic aciduria (MMA). We performed whole genome sequencing, transcriptomic sequencing, and mass spectrometry-based proteotyping from matched primary fibroblast samples of 230 individuals (210 affected, 20 controls) and related the molecular data to 105 phenotypic features. Integrative analysis identified a molecular diagnosis for 84% (177/210) of affected individuals, the majority (148) of whom had pathogenic variants in methylmalonyl-CoA mutase (*MMUT*). Untargeted analysis of all three omics layers revealed dysregulation of the TCA cycle and surrounding metabolic pathways, a finding that was further corroborated by multi-organ metabolomics of a hemizygous *Mmut* mouse model. Integration of phenotypic disease severity indicated downregulation of oxoglutarate dehydrogenase and upregulation of glutamate dehydrogenase, two proteins involved in glutamine anaplerosis of the TCA cycle. The relevance of disturbances in this pathway was supported by metabolomics and isotope tracing studies which showed decreased glutamine-derived anaplerosis in MMA. We further identified MMUT to physically interact with both, oxoglutarate dehydrogenase complex components and glutamate dehydrogenase providing evidence for a multi-protein metabolon that orchestrates TCA cycle anaplerosis. This study emphasizes the utility of a multi-modal omics approach to investigate metabolic diseases and highlights glutamine anaplerosis as a potential therapeutic intervention point in MMA.

Take home message: Combination of integrative multi-omics technologies with clinical and biochemical features leads to an increased diagnostic rate compared to genome sequencing alone and identifies anaplerotic rewiring as a targetable feature of the rare inborn error of metabolism methylmalonic aciduria.

Graphical abstract

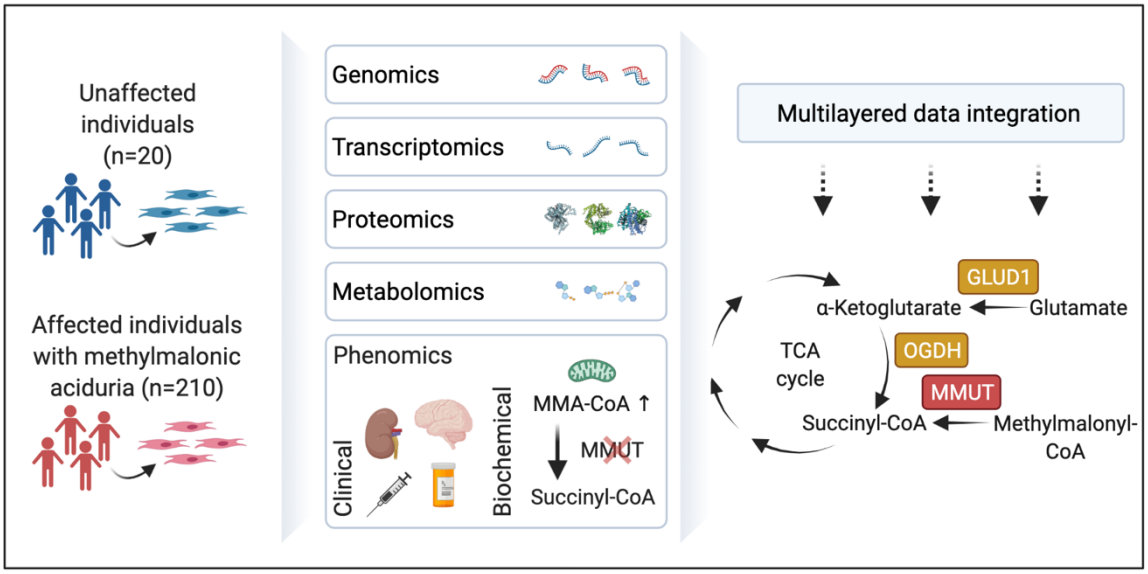

Keywords

Rare disease, inborn error of metabolism, multi-omics, RNA-seq, WGS, proteomics, methylmalonic aciduria

Main

Inborn errors of metabolism (IEMs), first described by Archibald Garrod [2], are inherited diseases resulting in inadequate function of metabolic proteins. IEMs represent a group of nearly 1,500 diseases with a combined incidence of approximately 1:800 births. They present a clinically and genetically heterogeneous picture making them inherently difficult to diagnose [3,4]. Beyond their diagnostic challenges, the pathomechanisms of many IEMs are not well understood, hence most IEMs lack rationalized treatment approaches [5].

Technological advances in genomics and mass spectrometry, leveraging datasets of whole molecule classes (omics), have recently led to a paradigm shift in their use as diagnostic tools. For example, single-layer whole genome sequencing has achieved diagnostic rates of 30-50% in rare disease cohorts [6–8], while dual-layer combination with RNA sequencing can improve this by 10-35% [9–12]. In spite of these advances a significant number of patients remain undiagnosed and disease course prediction remains poor, mainly due to a lack of pathomechanistic understanding and often unclear genotype-phenotype relationships.

Multi-layered omics data have the potential to not only increase diagnosis rates of inborn errors of metabolism, but also to uncover novel mechanistic insights into disease pathophysiology [1], thus potentially indicating new therapeutic targets. Such a combinatorial approach is key to move beyond the traditional “one gene – one disease” view of these disorders which fails to explain phenotypic heterogeneity based on genetic variation only. However, simultaneous application of multi-omics technologies for this purpose have not been rigorously tested, and their true utility as well as bottlenecks and knowledge gaps to using them in this regard remain unknown.

Here, we have generated multi-layered omics information from individuals suspected with the prototypic IEM methylmalonic aciduria (MMA). MMA has approximately 20 potential monogenic causes most of which result in deficiency of the methylmalonyl-CoA mutase (MMUT) enzyme due to loss of function or proper cofactor (cobalamin) assembly [13]. Even though the (dys)function of MMUT has been studied extensively [14–17], the main metabolic disturbances in MMA remain an open question.

By combining whole genome sequencing (WGS), whole transcriptome sequencing (RNA-seq) and proteotyping information (DIA-MS) with phenotypic features we identified disease causative and pathogenic features in a cohort of MMA affected individuals. We revealed underlying damaging variants and differentially expressed transcripts and proteins directly related to anaplerosis of the TCA cycle. Moreover, follow-up studies utilizing untargeted metabolomics and [U-^{13}C]glutamine tracing revealed a depletion of TCA cycle metabolites and decreased oxidation of glutamine-derived carbons in line with the identified dysregulation of glutamate dehydrogenase and oxoglutarate dehydrogenase enzymes, which we found to physically interact with MMUT. Beyond unveiling these metabolic disturbances in MMUT deficiency, our findings enable a better biological understanding of TCA cycle anaplerosis. Furthermore, the anaplerotic TCA cycle insufficiency may be a potential intervention point in MMA to therapeutically compensate for the loss of TCA cycle intermediates.

106 # Results

107 ## Monogenic disease variant detection through multi-omics

108 To extend the understanding of MMA from the causative genomic lesions to the affected biochemical
109 processes, we performed high-quality WGS, RNA-seq and DIA-MS based proteotyping on fibroblasts
110 taken from 230 individuals (210 affected by MMA, 20 unaffected), representing a mainly European
111 cohort collected over a 25-year period (**Fig. 1a** and **Extended data Fig. 1**). Classical MMA is caused
112 by defective processing of methylmalonyl-CoA in the catabolism of propionate, resulting from
113 deficiency of the enzyme methylmalonyl-CoA mutase (MMUT) or proteins related to production of
114 its cofactor adenosylcobalamin (e.g., MMAA, MMAB) or substrate (**Fig. 1a**). Biochemical assay of
115 propionate incorporation (PI) [18], and MMUT enzyme activity [14] strongly correlated across all samples
116 (rho=0.73, p<0.0001) (**Extended data Fig. 2a**). Fibroblasts from 150 individuals with MMA had
117 reduced MMUT activity (MMUT-deficient), including 123 which did not increase upon cofactor
118 supplementation (**Extended data Fig. 2b**, **c**), while those of 60 individuals had MMUT activity
119 similar to controls (other MMA) (**Fig. 1b**).

120 In the MMUT-deficient samples we searched the WGS dataset for disease-causing variations in the
121 *MMUT* gene and identified the molecular cause of disease in 148/150 individuals (**Extended data**
122 **Table 1**). Pathogenic variants constituted 165 missense alleles, 105 truncating alleles, 21 splicing
123 alleles, two alleles with in-frame deletions and three alleles containing copy number variants (**Fig. 1c,**
124 **d** and **Extended data Fig. 2d**), of which 41 variants were novel (**Extended data Table 1**). RNA-seq
125 identified reduced *MMUT* RNA expression in cells from MMUT-deficient individuals compared to
126 the other groups (**Fig. 1e**). Individuals with strongly reduced RNA expression were enriched for
127 splicing and/or truncating variants, consistent with nonsense-mediated decay (**Extended data Fig.**
128 **2e**). DIA-MS based proteome measurements revealed reduced MMUT protein levels in MMUT-
129 deficient primary fibroblasts (**Fig. 1f**) which was distributed across all variant types (**Extended data**
130 **Fig. 2e**). Consistent with its disease-causing role, MMUT RNA and protein levels were positively and
131 significantly associated with PI and MMUT activity (**Extended data Fig. 2f**) and MMUT represented

132 the most significantly dysregulated RNA and protein of MMUT-deficient samples when compared
133 against all other samples (**Fig. 1g** and **Extended data Fig 2g**).

134 In the remaining 60 samples, we identified bi-allelic disease-causing variants for 22 individuals in
135 genes other than MMUT: *ACSF3* (17 individuals) (**Fig. 1h**), *TCN2* (3 individuals), *SUCLA2* (1
136 individual), and MMAB (1 individual) according to the ACMG classification (**Extended data Table**
137 **1**). By searching RNA-seq for aberrantly expressed genes using OUTRIDER [19] (**Extended data Fig**
138 **3**), we identified two individuals with very low *ACSF3* expression; two with aberrant *SUCLA2*
139 expression, in whom we confirmed predicted splicing and copy number variants at the genomic level
140 (**Extended data Table 1**); two with very low *MMAA* expression, confirmed by complementation
141 analysis; and one with low *MMAB* transcript, also confirmed by complementation analysis. Therefore,
142 we identified a molecular cause for 29/60 remaining individuals (48%), including 18 pathogenic
143 mutations, of which 10 were novel (**Extended data Table 1**). In sum, we found a diagnosis for
144 177/210 (84%) affected individuals (**Fig. 1i**), including 150 with deficiency of MMUT and 19 with
145 damaging variants in *ACSF3* accounting for the largest cohort of ACSF3 deficiency.

146

147

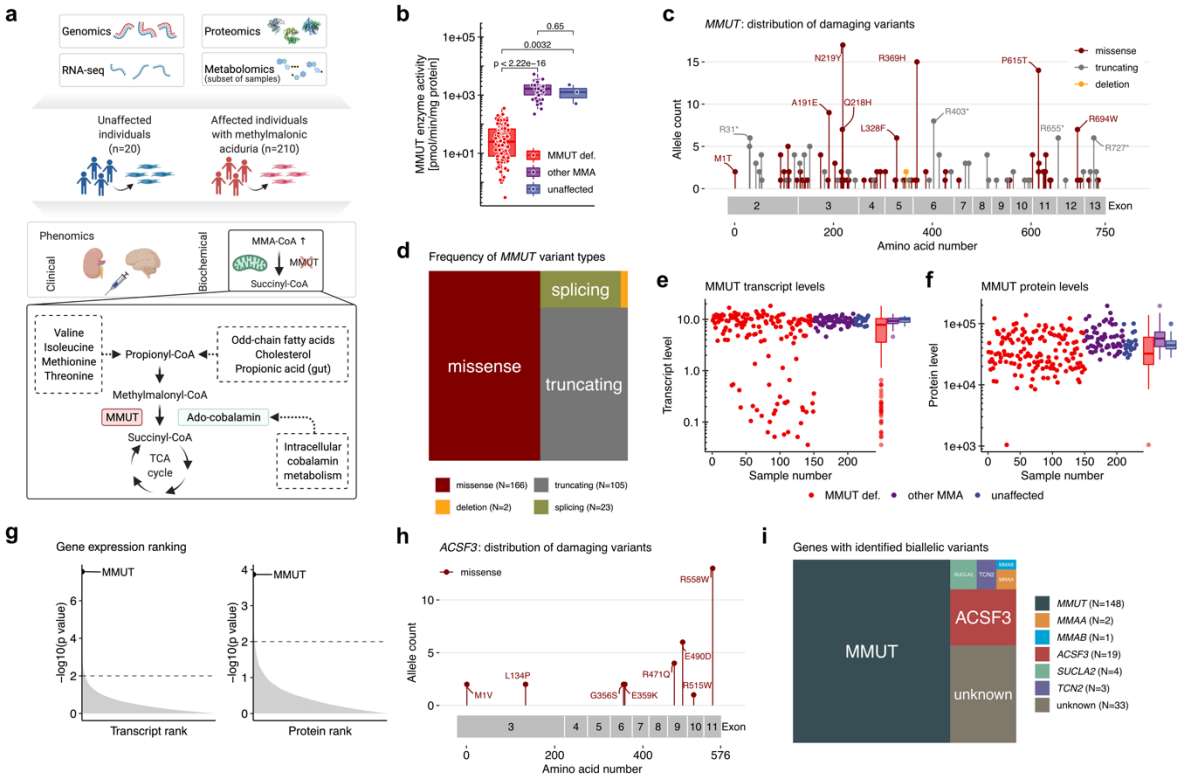

Fig. 1: Multi-facetted omics view enabled a molecular diagnosis in 84% of individuals. a, Study overview with depiction of the propionate pathway including its precursors and the pathways catalyzed by MMUT. **b**, MMUT enzyme activity per study sub cohort. **c**, Lollipop plot of all pathogenic variants found on the *MMUT* gene. **d**, Proportions of variant types as identified on the *MMUT* gene. **e**, Transcript levels of *MMUT* by study sub cohorts. **f**, MMUT protein levels divided in study sub cohorts. **g**, Gene ranks according to p-values as calculated by gene-wise Welch's *t*-test in the proteomics and transcriptomics data. **h**, Lollipop plot of pathogenic variants identified in *ACSF3*. **i**, Proportions of affected genes identified in the whole cohort.

Phenotypic description and association to disease severity

It was our expectation that the genetic underpinnings identified above would only partly predict the clinical and biochemical phenotypes of affected individuals. We therefore aimed at establishing a quantitative assessment of disease severity by converting the catalogue of mostly semantic phenotypic traits into key numeric variables. A correlation matrix of all phenotypic variables (n = 105), spanning clinical symptoms at presentation and during disease course (n = 53), clinical treatments and therapeutic response (n = 23), clinical chemistry of blood or tissues including metabolite measurements (n = 13), and *in vitro* biochemical parameters (n = 13), revealed a cluster of features (MMUT activity, PI) that showed strong correlation across many variables (**Fig. 2a**, **b**).

167 Since the identified few variables strongly associated with many clinical features, we postulated that
168 most disease characteristics might be well predicted by one or a select few variables. As proof-of-
169 principle, we established a clinical severity score (CSS), which incorporated the outcome of five
170 typical clinical features [20] (for composition see **Methods**), whereby a score of 0 represented absence
171 of these typical MMA features, a score of 1 mild MMA, and a score of 2 or higher (max. 5) moderate
172 to severe MMA disease. Comparison of the CSS against all phenotypic parameters demonstrated
173 significant correlation with 54 individual variables (**Fig. 2c**), including many classical phenotypic
174 symptoms of MMAuria, such as acidosis, hyperammonemia and muscular hypotonia as well as the
175 requirement for dietary and pharmacological interventions (**Extended data Fig. 4a**). Importantly, the
176 CSS also inversely correlated with age of onset (**Extended data Fig. 4b**), a parameter that on its own
177 has been used as an indication of clinical severity [21].

178 Multiple correlation analysis identified PI in the presence of hydroxocobalamin (PI+) to significantly
179 correlate to 41 phenotypic features, the most of any individual continuous variable (**Fig. 2c**). This
180 contrasts, for example, to age at onset which significantly correlated with only 17 parameters (**Fig.
181 2c**). Closer inspection revealed PI+ to be inversely correlated to disease severity, including significant
182 positive correlation with, e.g., glomerular filtration rate or age at disease onset, and negative
183 correlation with, e.g., methylmalonic acid concentration in plasma, presence of clinical interventions
184 such as protein restriction and the CSS (**Fig. 2d** and **Extended data Fig. 4c**, **d)**. Therefore, in line
185 with its validity as a diagnostic test for MMA [18], the PI+ variable was used as an approximation of
186 clinical disease severity in this study.

187

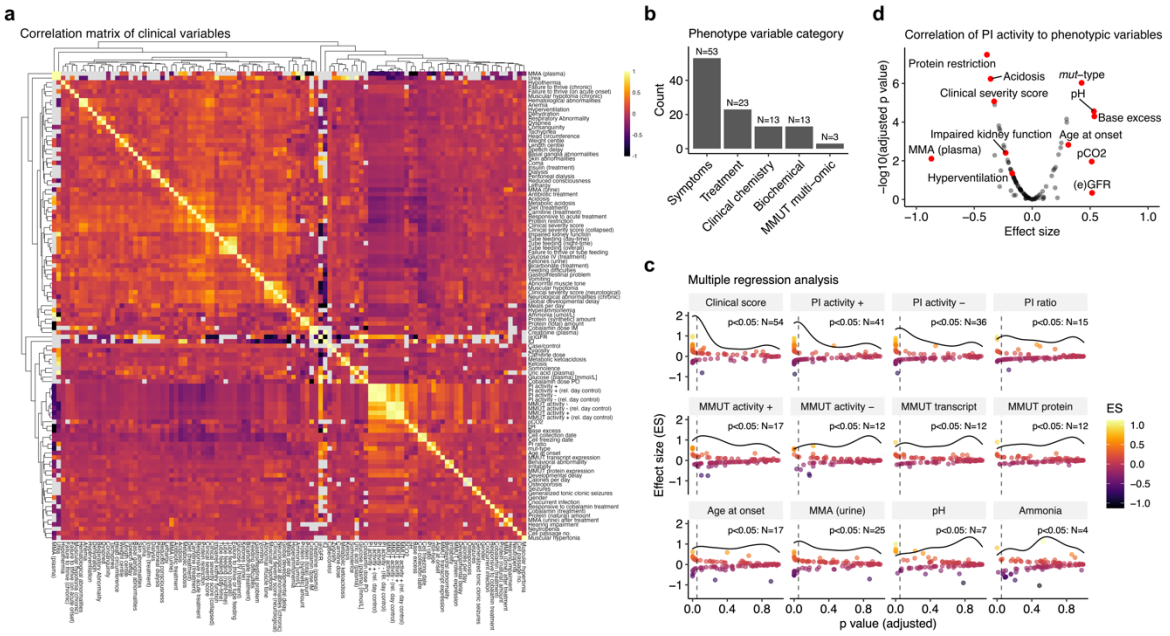

Fig. 2: Phenomics analysis reveals two main surrogate markers of disease severity (clinical severity score and PI+ activity). a, Correlation matrix of all continuous numeric and discrete phenotype variables. **b**, Number of phenotypic traits according to five phenotype subcategories. **c**, Panel of selected phenotypic traits and their overall strength of representing the entirety of the phenomics dataset (here termed clinical disease severity) as assessed by linear modelling. Each point represents the result of linear regression against one other phenotypic variable with the effect size on the y-axis and the resulting p-value on the x-axis. The horizontal curved line indicates the density of data points as distributed along the x-axis. Vertical dashed line indicates threshold of significance (p-value <0.05). **d**, Linear regression results of the PI+ activity variable compared against the rest of the phenotypic variables. Phenotypic traits available from **Source data Table 1**.

Multi-layered biology reveals disruption of TCA cycle and associated pathways

To identify disease-associated expression alterations of genes, proteins, and pathways, we attempted a global assessment of transcript and protein expression, integrated with the quantitative phenotype variables identified above. Since patients with TCN2, SUCLA2 and ACSF3 deficiency lack most of the typical signs and symptoms of classical MMA, we compared MMUT-deficient with all non-MMUT-deficient samples (control).

Investigation of transcripts and proteins using differential correlation patterns (Pearson correlation method), dimensionality reduction via Principal Component Analysis and DESeq2 did not immediately yield clear grouping of the data, nor obvious expression pattern differences between the groups (**Extended data Fig. 5a**, **b**, **c**). However, multi-omics factor analysis [22], integrating both

genetic data layers and proteotyping data, identified mitochondrial metabolic pathways and in particular the electron transport chain and the TCA cycle to be enriched in MMUT-deficient samples (**Fig. 3a**). In more detail, the proteins SLC16A3, CS, MDH2, and OGDH were found to be the main drivers of this particular factor's variance in the proteotyping data within the TCA-associated gene sets (**Fig. 3b**). Linear discriminant analysis of genes shared between transcriptomics and proteotyping indicated MMUT as the strongest and SUCLA2, OGDH, and PDHB to be top drivers of separation between MMUT-deficient and control samples (**Fig. 3c**). Further, gene set enrichment analysis utilizing sample stratification by disease severity, both by CSS and PI+, also identified oxidative phosphorylation and the TCA cycle as over-represented pathways in the proteomics (CSS and PI+) and transcriptomics (CSS) datasets (**Fig. 3d**).

The biological relevance of these changes was confirmed in a hemizygous mouse model of MMA [23] (**Fig. 3e**). Untargeted metabolomics of brain, heart, kidney, liver, plasma, and urine confirmed elevated levels of the eponymous metabolite methylmalonic acid in mutant animals, while pathway enrichment analysis pointed to dysregulated TCA cycle pathways in all tissues and urine (**Fig. 3f**). Transcriptomics of brain tissue further confirmed the expected 50% reduction in *Mmut* transcript of mutant mice, along with enrichment of electron transport chain and oxidative phosphorylation pathways (**Fig. 3g** and **Extended data Fig. 6**).

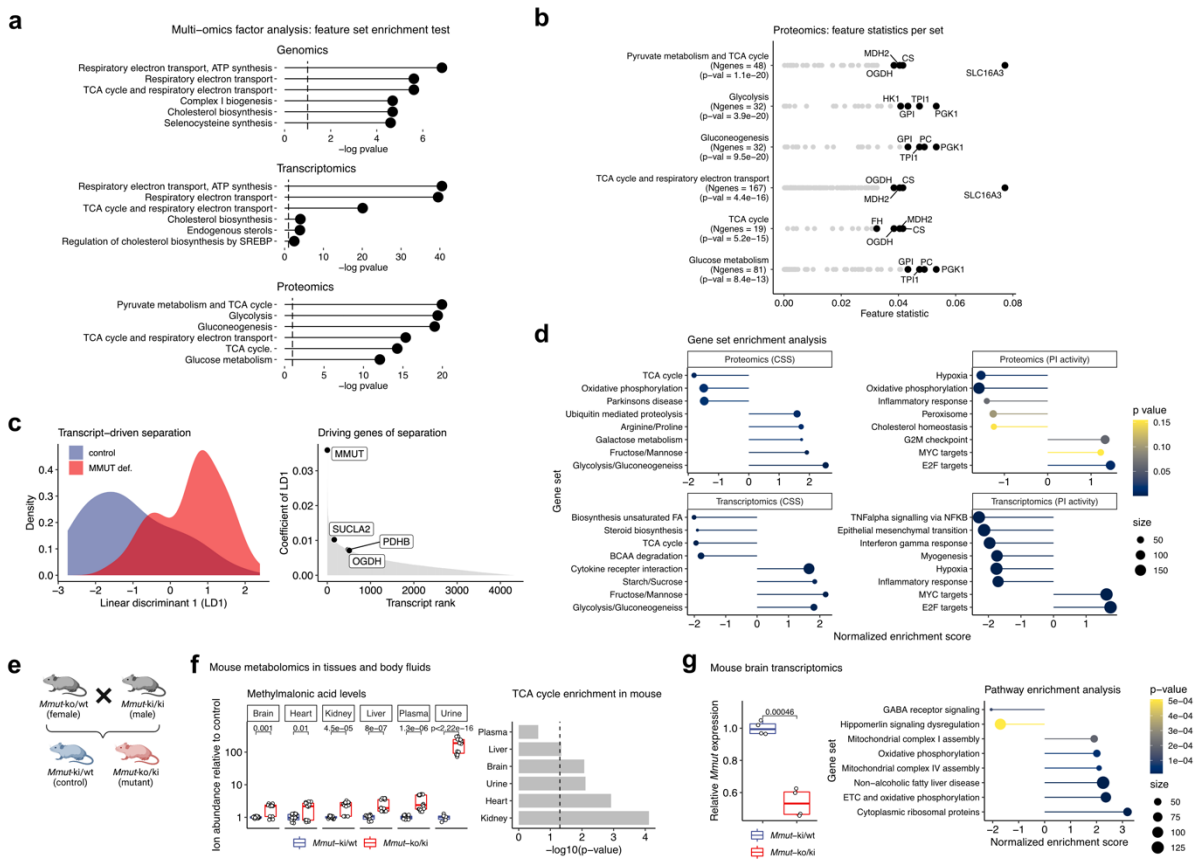

Fig. 3: Untargeted integration of omics data layers highlights the TCA cycle and associated pathways as well as oxidative phosphorylation gene sets to be dysregulated in MMA. a, Gene set enrichment test using the multi-omics factor analysis tool (MOFA). **b**, Detailed feature statistics of the top enriched gene sets following MOFA in the proteomics data. **c**, Linear discriminant model (split to assign training and test data: 0.5) of transcripts separates MMUT-deficient from control driven by *MMUT* and other genes related to the TCA cycle. **d**, Gene set enrichment analysis based on effect size ranking derived from differential expression analysis (also see **Fig 4b**). **e**, Breeding scheme of *Mmut* deficient mice. **f**, Untargeted metabolomics in mouse tissues and body fluids, depicting boxplots for methylmalonic acid and metabolite set enrichment analysis based on the complete metabolomics dataset. **g**, RNA-seq on mouse brain tissue. Boxplots of the relative *Mmut* transcript abundance and gene set enrichment analysis following DESeq2 analysis, dot size represents number of genes per set.

MMUT deficiency leads to transcript and protein alterations in proximal enzymes

Since both data-driven and phenotypically stratified analyses indicated TCA and associated pathways to be disrupted in disease, we performed a concerted investigation of the TCA cycle enzymes, including those which metabolize anaplerotic (replenishing TCA cycle intermediates) and cataplerotic (removing TCA cycle intermediates) reactions, from which we had both RNA and protein

information. As controls we included isoforms of TCA enzymes which are not involved in these pathways (**Fig. 4a**). Direct comparison of RNA and protein expression between MMUT-deficient and control cells revealed MMUT to be significantly dysregulated (**Fig. 4a outer band**).

Differential expression analysis, performed using a linear mixed modelling approach [24], identified the genes with the strongest effect size and significance to be enriched for mitochondrial localization, as listed in MitoCarta 3.0 [25] (**Extended data Fig. 7a**). Closer examination (**Fig. 4a middle band, b**), identified MMUT to be significantly downregulated in disease at both the RNA and protein level, while ALDH2, which catalyzes the interchange between methylmalonate and methylmalonate semialdehyde, was in contrast upregulated in both. A further upregulated transcript was *PDK4* (**Fig. 4b**), which is responsible for the phosphorylation and as a consequence inactivation of the pyruvate dehydrogenase complex. However, the proteins with the overall largest effect size were OGDH (downregulated in disease) and GLUD1 (upregulated in disease), both enzymes involved in the anaplerosis of glutamine (**Fig. 4b**).

Examination of RNA-protein expression correlation in all samples revealed a limited Spearman correlation of 0.14 at the gene level (4318 transcript-protein pairs) and 0.40 at the sample level (**Fig. 4c** and **Extended data Fig. 8a**), similar to findings by others [26]. Comparison of RNA-protein correlation in MMUT-deficient cells compared to controls revealed that, while 1158 pairs (26.8%) correlated significantly (p-value < 0.05) in both genotypes (**Fig. 4d** all colored points and **Extended data Fig. 8b**) in accordance with previous studies [27], the correlation of some genes segregated depending on the genotype (MMUT-deficient vs control) (**Fig. 4d**). In particular, OGDH, GLUD1, CS, and GLS showed higher RNA-protein correlation in MMUT-deficient samples than controls, while SUCLA2 had reduced RNA-protein correlation (**Fig. 4a**, **d** and **Extended data Fig. 8c**). OGDH and SUCLA2 were among the genes with the strongest genotype-dependent RNA-protein correlation changes (**Fig. 4d**). Interestingly, we found poor RNA-protein correlation for MMUT in both control and MMUT-deficient cells (**Fig. 4a**, **d** and **Extended data Fig. 8c**).

Finally, MMUT protein levels positively correlated to protein levels of many TCA and anaplerotic enzymes in control but not in MMUT-deficient cells**,** while there was little or no protein expression

correlation between MMUT and non-TCA protein isoforms in either genotype (**Fig. 4a center** and **Extended data Fig. 8d**). Such a relationship is exemplified by MMUT:ACO2 and MMUT:ACO1 (**Fig. 4a center** and **Extended data Fig. 8e**) and provides the first indication that MMUT may be part of a so far unknown interaction network with these mitochondrial TCA cycle and anaplerotic enzymes [28]. Examination of pairwise correlation between all proteins and transcripts (**Extended data Fig. 8f, g**) in these pathways suggests that TCA cycle and anaplerotic enzymes have a positive correlation with each other, which is not altered in MMUT deficiency, unless MMUT is included in the comparison. Overall, the above findings suggest that disruption of MMUT RNA and protein expression drives regulatory changes in certain TCA and anaplerotic enzymes.

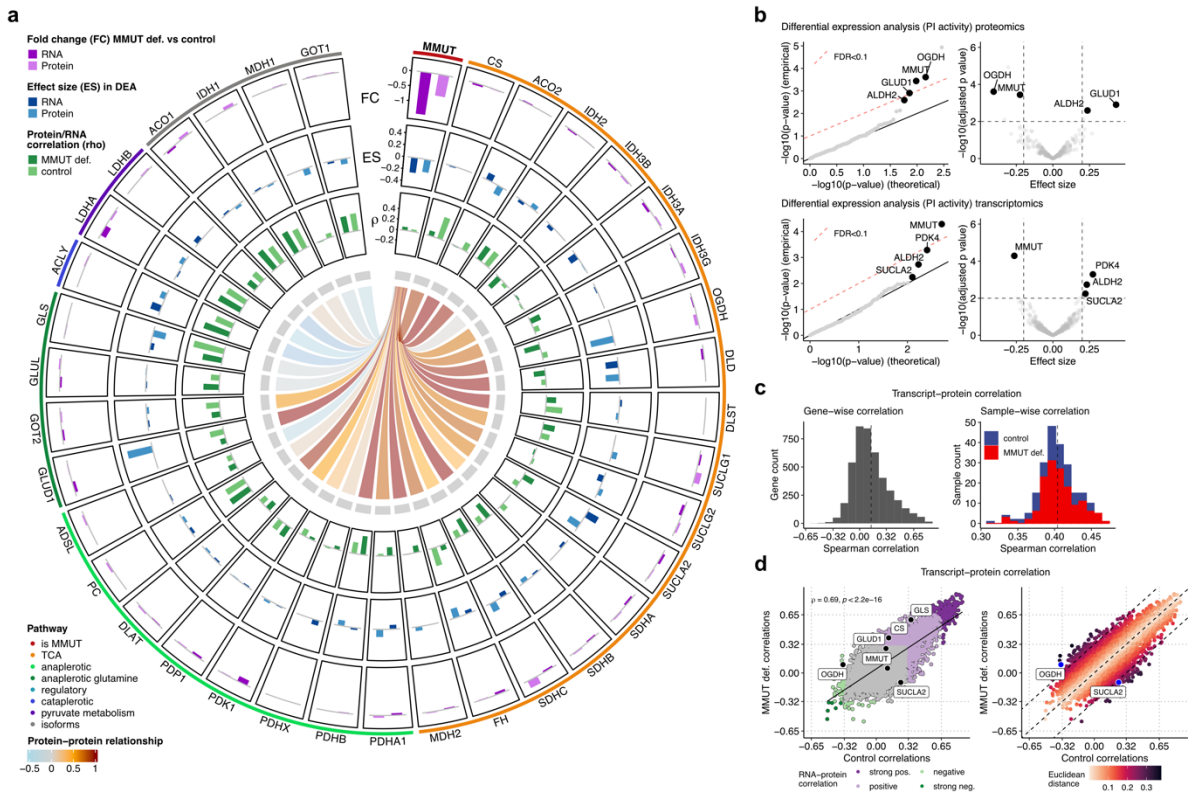

Fig. 4: Transcript-protein and protein-protein correlation analyses reveal coordinated relationships between MMUT and TCA genes and proteins but not their isoforms. a, Circos plot depicting raw fold changes of transcripts and proteins, effects sizes derived from differential expression analysis, transcript-protein correlations, and correlative relationships of the MMUT protein to TCA proteins and their corresponding isoforms. **b**, Q-Q and volcano plots illustrate the results of the differential expression analysis based on a linear mixed modeling approach applied to the proteomics and transcriptomics data, restricted to enzymes (or their encoding genes) localized in the mitochondria. **c**, Histograms of Spearman correlations across 4318 transcript-protein pairs (left), and 221 samples (right). **d**, Scatter plot of Spearman correlations in MMUT-deficient against control. Euclidean distance from the diagonal is calculated based on the formula |(MMUT def. correlation – control correlation)|/sqrt(2).

295

296 Metabolomics highlights rewiring of TCA cycle anaplerosis

297 To examine the functional consequences of the above RNA and protein expression alterations, we
298 performed untargeted metabolomic analysis on a set of 6 MMUT-deficient and 6 control primary
299 fibroblasts derived from unaffected individuals (for selection criteria, see **Extended data Fig. 9a** and
300 **Methods**). Among the most significantly changed metabolites we found decreased glutamine and
301 alanine as well as increased hexoses, methylcitrate, oxoadipate, aminoadipate, and pyruvate (**Fig. 5a**).
302 Combining these alterations with observed changes in RNA and protein expression in the same
303 samples provides insight into disruption of TCA cycle anaplerosis in MMUT deficiency (**Fig. 5b**).

304 The increased pyruvate level (**Fig. 5a, c**), increased expression of the PDH complex inhibitor *PDK4*
305 (**Fig. 4b**), and strongly elevated 2-methylcitrate (**Fig. 5c**), a biomarker of MMA formed by citrate
306 synthase mediated mis-condensation of oxaloacetate with propionyl-CoA instead of acetyl-CoA,
307 together suggest reduced incorporation of pyruvate into the TCA cycle. This is further supported by
308 the analysis of our cross-dimensional data which identified stronger pyruvate to *PDHB* transcript and
309 pyruvate to PDHX protein correlations (**Fig. 5d**), implying reduced pyruvate turnover per transcript
310 and protein respectively. Consecutive metabolites in a pathway often correlate strongly [27], here
311 exemplified by malate and fumarate (**Fig. 5d**). Although we found such a correlation between
312 pyruvate and its downstream metabolite (iso)citrate in both control and MMUT-deficient cells, our
313 data suggests that in MMUT-deficient cells a higher concentration of pyruvate is required to create the
314 same amount of (iso)citrate as controls (**Fig. 5d**), again supporting reduced incorporation of pyruvate
315 into the TCA cycle.

316 Despite this reduced pyruvate-mediated anaplerosis, 2-oxoglutarate, succinate, fumarate and malate
317 levels remained unchanged in MMUT-deficient cells (**Fig. 5c** and **Extended data Fig. 9b**),
318 suggesting stable TCA cycle metabolite pools in these primary fibroblast cells. As our previous
319 findings indicated altered proteins in glutamine anaplerosis (**Fig. 3b, c, 4a**), we investigated the
320 contribution of this pathway towards the balance of the TCA cycle. Glutamine strongly correlated

321 with glutamate in both MMUT-deficient and control samples (**Fig. 5d**). However, in MMUT-deficient
322 cells, glutamine and glutamate were decreased (**Fig. 5c**), and there was a negative correlation of
323 glutamate with 2-oxoglutarate, suggestive of more tightly regulated glutamine flux under disease
324 conditions (**Fig. 5d**). Abrogated positive correlation of glutamate and aspartate potentially points to an
325 altered dependence on glutamate for TCA cycling but not production of cataplerotic metabolites, such
326 as aspartate (**Fig. 5d**). In line with this, we found an inverse relationship between *MMUT* transcript
327 and 2-oxoglutarate in MMUT-deficient cells (**Fig. 5d**). While we focused our efforts on the
328 investigation of TCA anaplerosis at this stage, the power of our untargeted dataset was further
329 illustrated by more unexpected findings, including increased oxoadipate and aminoadipate (**Fig. 5a**),
330 upstream metabolites of 2-oxoadipate dehydrogenase complex which shares its E2 (DLST) and E3
331 (DLD) components with 2-oxoglutarate dehydrogenase complex (**Extended data Fig. 9c**), suggestive
332 of a preference for 2-oxoglutarate over 2-oxoadipate metabolism.

333 The above results point to an adjusted reliance on the glutamine anaplerotic pathway in disease; a
334 hypothesis we tested further by assessing relative carbon incorporation derived from anaplerotic
335 glutamine into TCA cycle and associated intermediates using MS-based stable isotope tracing. For
336 this experiment, control (wildtype, WT), *DLST*-KO, and *MMUT*-KO 293T cells, validated by Western
337 blotting and enzyme activity measurements (**Extended data Fig. 10**), were cultured in glutamine-free
338 glucose-DMEM supplemented with [U-^{13}C]glutamine. *DLST*-KO cells were used as a control to
339 mimic the above detected reduction of OGDH protein in MMUT deficiency, allowing us to assess
340 fractional incorporation of glutamine into TCA cycle intermediates when the oxidative pathway
341 (clockwise from 2-oxoglutarate, **Fig. 5e**) is completely blocked (DLST is a component of the 2-
342 oxoglutarate dehydrogenase complex, metabolizing 2-oxoglutarate to succinyl-CoA). By analyzing
343 the pool sizes, we could confirm reduced levels of glutamine and glutamate (**Extended data Fig. 11a**)
344 comparable to the patient fibroblasts (**Fig. 5c**), validating our experimental model. In addition, we
345 found markedly reduced TCA cycle metabolites, including citrate, fumarate, malate, succinate, and
346 aspartate (a proxy for oxaloacetate [29]), indicating an overall reduced TCA metabolite pool in MMUT
347 deficiency, while KO of *DLST* led to virtual absence of most TCA cycle metabolites (**Fig. 5f**). To

348 identify differential labeling patterns, we studied the isotope distribution based on the relative
349 incorporation of glutamine-derived carbons and found a decreased proportional fraction of M+4
350 isotopologues under *MMUT*-KO conditions for all studied TCA cycle metabolites and aspartate (**Fig.**
351 **5g**, **Extended data Fig. 11b**), suggesting reduced derivation from glutamine. Indeed, we found a
352 decreased fractional contribution of glutamine to the TCA cycle for all studied intermediates (**Fig.**
353 **5h**). Moreover, consistent with reduced OGDH activity, there was a relative preference for the
354 reductive TCA cycle pathway, as indicated by an increased M+5/M+4 ratio for citrate [30,31] in MMUT
355 deficiency (**Extended data Fig. 11c**). In sum, this suggests there is reduced production of TCA cycle
356 intermediates which is not compensated for by glutamine anaplerosis.

357

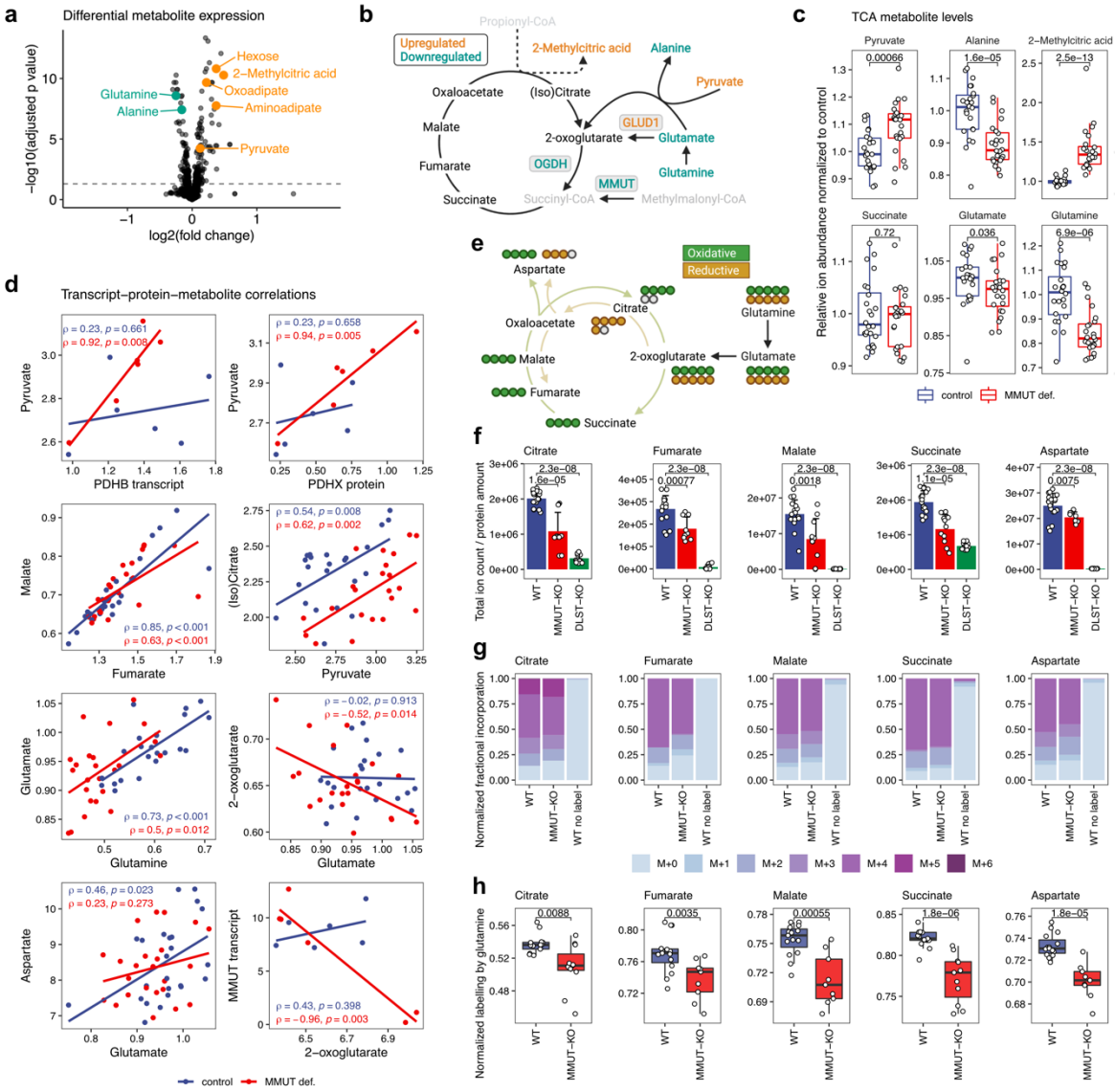

Fig. 5: Polar metabolomics in selected patient fibroblasts and glutamine tracing studies in CRISPR/Cas9 KO 293T cells highlight differential glutamine anaplerosis. a, Volcano plot depicting differentially expressed metabolites. Highlighted are the ones particularly relevant to this study. **b**, Schematic depiction of the TCA cycle and relevant anaplerotic reactions. The color code indicates dysregulations on metabolite and protein level; grey metabolites were not detected. **c**, Boxplots to compare relevant TCA cycle metabolites, including the pathologically relevant biomarker 2-methylcitrate formed upon condensation of oxaloacetate with propionyl-CoA. **d**, Pearson correlation of a certain key metabolite against a metabolite, transcript, or protein variable. **e**, Schematic representation of labeling of TCA cycle and associated metabolites derived from labelled glutamine via anaplerosis. Circles represent carbon atoms. **f**, Pool sizes of metabolites in control and CRISPR/Cas9 KO 293T cells. **g**, Relative abundance of isotopologues after glutamine labelling. **h**, Relative fractional incorporation of labelled glutamine into TCA cycle and associated metabolites. All p-values are calculated by Wilcoxon rank test.

373 ## MMUT physically interacts with 2-oxoglutarate dehydrogenase and other
374 anaplerotic enzymes

375 The above observed adjustments in glutamine anaplerosis have an unclear regulatory etiology. Based
376 on the strong protein expression correlation between MMUT and proximal TCA cycle and anaplerotic
377 enzymes (**Fig. 4a** and **Extended data Fig. 8d)**, we hypothesized that these proteins may be part of a
378 shared metabolon complex, potentially facilitating regulation of TCA cycle anaplerosis of glutamine
379 by protein-protein interactions [28]. To gain insights into this potential physical relationship, we took
380 advantage of over-expression of C-terminally flag-tagged versions of MMUT, two pathway members
381 (MMAB and MCEE) expected to participate in any multi-protein complex containing MMUT, and
382 two negative controls (VLCAD and empty vector) in 293T cells (**Fig. 6a**). Using cross-linking affinity
383 purification coupled to mass spectrometry, at 1.0% FDR using 2 peptides minimum at 95% threshold,
384 each of these 'bait' proteins pulled-down a total of 100-350 different 'prey' proteins over 3 biological
385 replicates (**Fig. 6b**). Within this intersection, we identified 57 prey proteins pulled down by MMUT,
386 MMAB and MCEE in at least one replicate, but not by empty vector or VLCAD in any replicate (**Fig.**
387 **6b**).

388 Analysis of variance (ANOVA) of the biological triplicates comparing MMUT with EV and VLCAD
389 identified 22 proteins to be significantly enriched (nominal p-value <0.05) in the MMUT sample (**Fig.**
390 **6c** and **Extended data Table 2**). All proteins were designated by Uniprot to have mitochondrial
391 localization and included GLUD1, GOT2 and DLST (**Fig. 6c**). ANOVA comparing the intersection of
392 proteins confidently pulled down by all three of MMUT, MMAB and MCEE but not of EV or
393 VLCACD identified 11 MMUT/MMAB/MCEE interacting proteins, including GLUD1 and GOT2;
394 while the intersection of two of MMUT, MMAB, and MCEE against both negative controls identified
395 13 proteins which interacted with MMUT/MMAB, MMUT/MCEE or MMAB/MCEE, including
396 DLST (**Fig. 6d** and **Extended data Table 2**). Interaction of MMUT and DLST was further confirmed
397 by Western blot analysis (**Fig. 6e** and **Extended data Fig. 12ab**). These data indicate that MMUT
398 physically interacts with GLUD1 and the oxoglutarate dehydrogenase complex component DLST and
399 suggests that disruption of this interaction may underlie their altered regulation in disease.

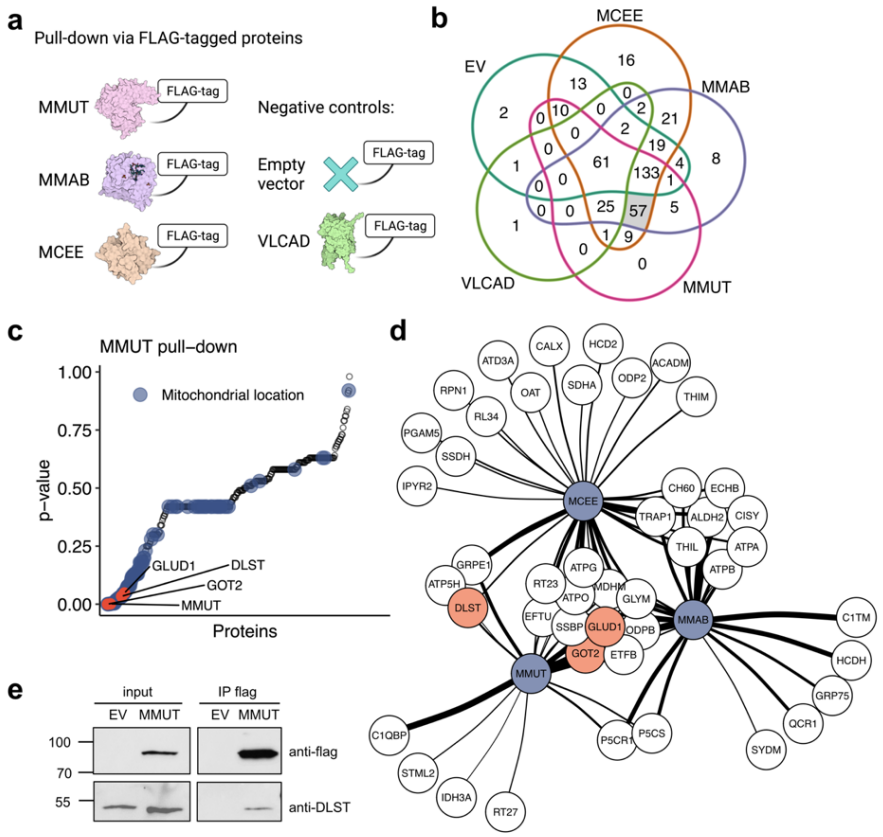

Figure 6. MMUT interacts physically with GLUD1, DLST, and GOT2 as demonstrated by FLAG-tag pull-down. a, Outline of experimental and control groups indicating which protein was used with a FLAG-tag in a cross-linking affinity purification experiment coupled to subsequent analysis of the pull-down samples by mass spectrometry. **b**, Venn diagram of proteins pulled down by the different flag-tagged proteins. **c**, ANOVA p-values of all proteins pulled down by MMUT. Blue dots indicate proteins with mitochondrial location according to Uniprot. **d**, Interaction network of significantly enriched proteins (ANOVA p-value < 0.05). Thicker connector indicates lower p-value. **e**, Western blot of immunoprecipitation of flag-tagged MMUT probing for DLST.

411 # Discussion

412 In this study, we used an integrated multi-modal approach to diagnose and uncover new
413 pathomechanisms of the inborn error of metabolism MMA. Unique to this investigation was the large
414 set of patient samples along with corresponding phenotypes available, and the ability to coordinate
415 aliquots from the same samples to generate data at three molecular layers. The results of our study
416 will encourage future endeavors to use our approach in any setting of an inborn monogenic disease.
417 Moving forwards, the datasets derived from our study can be further exploited, e.g., by applying
418 network contextualization tools [32], integrating multi-omics and flux modeling [33], and reconstructing
419 genome-scale metabolic networks [34], continuing to refine the pipeline of a multi-modal study of
420 inborn errors of metabolism.

421 Our findings reinforce the value of comprehensive and complementary datasets to increase diagnostic
422 yield and the understanding of the pathophysiological underpinnings of disease. Our multi-modal
423 profiling allowed the identification of causative genetic variation in 84% of the cohort, including
424 causative factors in the samples without MMUT deficiency. We were able to widen the set of genes
425 beyond the classical MMA genes *MMUT*, *MMAA*, and *MMAB*. For example, the identification of
426 *ACSF3* damaging variants in our cohort is particularly interesting as they have recently been linked to
427 combined malonic and methylmalonic aciduria (CMAMMA) [35]. The phenotype of CMAMMA
428 patients was indistinguishable from the remainder of MMA patients with normal MMUT activity,
429 highlighting the fact that inborn errors of metabolism present with widely overlapping phenotypes and
430 that they should be studied with large gene panels or with WGS approaches to avoid biases towards
431 known genes and to augment the chances of diagnosis.

432 While the ability of clinical phenotypic information to predict a molecular diagnosis was limited,
433 phenotypic variables – both clinical and biochemical – enabled sample stratification by disease
434 severity and consequently identification of multi-level alterations of metabolic genes/proteins which
435 were not apparent following examination of single omics layers. Such a move away from "data silos"
436 into true integrative and mechanism-based multi-layered analysis remains challenging, as it requires
437 new analytical and statistical methods to combine these disparate data sets [36]. In this capacity, multi-

omics factor analysis [22] highlighted the disruption to transcripts and proteins of the TCA cycle and related pathways, a finding verified by the correlation with phenotypic data utilizing both propionate incorporation activity and a clinical severity score. Following multi-modal integration, we performed metabolomics in select patient cells and further complemented the data with glutamine tracing and protein-protein interaction studies in a second cell model. In sum, these experiments showed decreased TCA metabolite pools and a reduced glutamine-derived anaplerosis, in line with the detected reduction of OGDH. In addition, we identified a list of novel MMUT-interaction candidates, among which DLST (OGDH complex component) and GLUD1 are directly involved in the glutamine anaplerotic pathway. Abrogation of the interaction with MMUT, due to *MMUT* knockout, could explain the reduction of glutamine anaplerosis. It is of note, that such a tailored set of follow-up experimental approaches – orthogonal to multi-omics data – is invaluable for molecular assessment of potential targets and the validation of their biological significance.

Overall, our results highlight the importance of the loss of methylmalonyl-CoA as an anaplerotic source and indicate a relevant reduction of TCA cycle intermediates in MMA, in part due to reduced anaplerotic supply stemming from glutamine. For the first time we show anaplerotic insufficiency in MMA and propose this phenomenon as a novel therapeutic target. Anaplerotic stimulating approaches have precedent in IEMs, including application of triheptanoin in long-chain fatty acid oxidation disorders [37]. Unfortunately, since fatty acid β-oxidation produces two acetyl-CoA and one propionyl-CoA per heptanoate molecule, use of this particular compound in MMUT deficiency is not feasible. However, anaplerotic treatment of patients suffering from the MMA-related disorder propionic aciduria with the TCA cycle intermediate citrate has been attempted, with inconsistent results [38]. Based on our findings, compounds such as dimethyl oxoglutarate, a membrane-permeable alternative to 2-oxoglutarate, previously used in a model of OXPHOS dysfunction [30], may represent a more promising therapeutic strategy. Studies to delineate the efficacy of such approaches in preclinical and clinical models will be important for the ongoing development of new treatments for MMA and inborn errors of metabolism in general.

465 # Acknowledgements

466 This project was funded by the ETH domain strategic focus area "Personalized Health and Related
467 Technology" (PHRT; https://www.sfa-phrt.ch). This work received financial support from the Swiss
468 National Science Foundation [31003A_175779] to M.R.B. and [310030_192505] to D.S.F. and from
469 the University Research Priority Program of the University of Zurich (URPP) ITINERARE—
470 Innovative Therapies in Rare Diseases. P.F. was supported by the Filling the Gap grant awarded by
471 the Medical Faculty, University of Zurich, Switzerland. We acknowledge the Functional Genomics
472 Center Zurich of the University of Zurich for RNA sequencing of the mouse brain tissues and
473 bioinformatics support as well as for support with the glutamine isotope studies.

474

475 # Author Contributions

476 Conceptualization, I.X., R.A., G.R., E.D., B.W., M.R.B., D.S.F.; Methodology, P.F., X.B., D.L.,
477 W.S., T.P., M.F., L.S., C.H., R.J.M., S.C., S.G., A.v.D., K.H., P.P., N.Z.; Investigation/Data analysis,
478 P.F., X.B., D.L., W.S., T.P., C.F., A.B., S.C., M.P., S.G., P.P., F.T., N.Z., G.R., D.S.F.; Writing –
479 Original Draft, P.F., D.S.F.; Writing – Review & Editing, all co-authors; Visualization, P.F., X.B.,
480 D.L., W.S., C.F.; Supervision, P.F., K.H., P.P., F.T., I.X., G.R., E.D., B.W., D.S.F.; Project
481 Administration, P.F., B.W.; Funding Acquisition, R.A., B.W., M.R.B., D.S.F.

482

483 # Declaration of interests

484 The authors declare no competing interests.

485

Extended data

Supplementary figures and tables in separate files.

Source data

Source data Proteomics

All mass spectrometry proteomics raw files have been deposited to the ProteomeXchange Consortium via the MassIVE partner repository (https://massive.ucsd.edu) with the dataset identifier MSV000088791.

Source data Metabolomics

Metabolomics mass spectrometry raw data for human fibroblast measurements have been uploaded to the MassIVE data repository (https://massive.ucsd.edu) with the dataset identifier MSV000089082.

Source data Affinity capture mass spectrometry raw data

IP-MS raw files have been deposited to the ProteomeXchange Consortium via the MassIVE partner repository (https://massive.ucsd.edu) with the dataset identifier MSV000088791.

Source data Quantitative Proteomics Data

CSV file containing the quantitative proteomics data used for the analyses.

Source data Quantitative Transcriptomics Data

CSV file containing the quantitative RNA-seq data used for the analyses.

Source data Table 1 Phenotypic dataset

CSV file containing all clinical information.

506 ### Source data Table 2 Pull-down

507 Complete list of proteins that were pulled down in the affinity capture mass spectrometry experiment.

508

509 # Methods

510 ## Cohort and patient-derived fibroblast samples

511 Primary fibroblast samples and corresponding disease-related information, including clinical and
512 diagnostic data, was collected from 1989 to 2015. The information was obtained and used under the
513 ethics approval granted by the Ethics Committee of the Canton of Zurich, Switzerland (no. KEK-
514 2014-0211, amendment: PB_2020-00053). Upon collection, primary fibroblasts were cultured using
515 Dulbecco's modified Eagle medium (Gibco, Life Technologies, Zug, Switzerland) with 10% fetal
516 bovine serum (Gibco) and antibiotics (GE Healthcare, Little Chalfont, UK) and either used
517 immediately, or exchanged to 90% fetal bovine serum and 10% dimethyl sulfoxide and stored in
518 cryovials under liquid nitrogen. A frozen aliquot of each primary fibroblast cell culture was sent for
519 WGS, RNA-seq and DIA-MS analysis (**Fig. 1a**). RNA-seq and DIA-MS were always performed from
520 matched aliquots.

521 ## Clinical disease severity score

522 The clinical disease severity score was based on five typical clinical signs/symptoms of MMA [20],
523 including age at disease onset, as well as the presence of neurological abnormalities, kidney
524 impairment, hematological abnormalities, and failure to thrive. Each patient was assigned a score
525 from 0-5 indicating increasing disease severity (**Source data Table 1**).

526 ## Biochemical assays

527 Propionate incorporation into acid precipitable material of primary fibroblasts was assessed according
528 to a protocol described previously [39] with modification as described [18]. Methylmalonyl-CoA mutase

529 enzyme activity assay was performed in crude cell lysates as originally described [40,41] using recent
530 modifications [14].

531 Whole genome sequencing

532 Genomic DNA was isolated using the QIAmp DNA Mini Kit reagents (Qiagen; Hilden, Germany)
533 following the protocol provided by the supplier. DNA was quantified by Qubit (Thermo Fisher;
534 Waltham, USA). Whole genome sequencing libraries were prepared with the TruSeq DNA PCR-free
535 library reagents (Illumina; San Diego, USA) using 1ug of genomic DNA following the protocol
536 provided by the supplier. The genomic DNA libraries were quantified using the KAPA Library
537 Quantification Complete Kit (Roche; Basel, Switzerland) according to the protocol supplied with the
538 reagents. The quantified libraries were sequenced on the NovaSeq 6000 sequencer (Illumina) using a
539 150-nucleotide paired end run configuration following the protocol provided by the supplier.

540 RNA sequencing

541 Total RNA was isolated using the RNeasy Plus Mini Kit (Qiagen). The total RNA was quantified
542 using the Qubit (Thermo Fisher) and quality-controlled using the Fragment Analyzer (Agilent, Santa
543 Clara, USA). RNA-seq libraries were prepared using the TruSeq Stranded mRNA-seq reagents
544 (Illumina) using 200ng of total RNA following the protocol provided by the supplier. The quality of
545 the RNA-seq libraries was assessed on Fragment Analyzer (Agilent) and the libraries were quantified
546 using the Qubit (Thermo Fisher). The libraries were sequenced on Illumina HiSeq 4000 using the 75-
547 nucleotide paired end run configuration following the protocol provided by the supplier.

548 Sample preparation for mass spectrometry proteotyping measurements

549 Samples were processed in blocks of 8 taking into consideration a balance between disease types and
550 control samples. All other factors within a block were randomized. 230 samples were processed in
551 three batches. For sample processing, aliquots of primary fibroblast (~1e6 cells per vial, frozen in
552 either DMEM or FBS or a mix of DMEM/FBS, plus 10% DMSO) were washed twice in ice-cold PBS

553 (Gibco). After centrifugation for 5 minutes at 300g, the cells were resuspended in lysis buffer
554 (Preomics) at a ratio of 1:1 (vol pellet/vol lysis buffer) and incubated at 95°C for 10 mins. Samples
555 were sonicated in a vial tweeter (Hielscher Ultrasound Technology) at 4°C for 3 cycles with an
556 amplitude 100%, power 80% during 30 secs. For each sample, the total protein concentration was
557 estimated by nanodrop. 100 ug of protein lysate were further processed with the iST kit (Preomics).
558 The purified peptides were resuspended in LCLoad buffer containing iRT peptides (Biognosys) at a
559 concentration of 1 ug/ul.

560 Spectral library generation

561 For spectral library generation, three times 24 samples (3x8 sample blocks) were pooled. Pooled
562 sample batches were digested as described above. 100 µg of purified peptides were fractionated on a
563 C18 column (YMC-Triart, C18, 3µm, 250 x 0.5 mm ID) according to pH on an Agilent HPLC 1260
564 system with a stepped 61 min gradient ranging from 95 % buffer A (20 mM ammonium formate
565 acid/H2O) to 85% buffer B (20 mM ammonium formate/90 % ACN). 48 fractions were collected per
566 sample and subsequently pooled to 24 fractions. Samples were resuspended in 5% ACN/0.1% FA and
567 analyzed on a QExactive HF-X mass spectrometer (Thermo Fisher Scientific) in DDA mode. The
568 same nLC 1200 configuration and mobile phase gradient elution conditions as for DIA were applied.

569 Full MS survey scans were acquired at a resolution of 60,000 with automatic gain control (AGC)
570 target of 3e6 and a maximum injection time of 45 ms over a scan range of m/z 375-1500. A data-
571 dependent top 12 method was used for HCD MS/MS with a normalized collision energy of 28 at a
572 resolution of 15,000 and a fixed first mass of m/z 100. Precursor ions were isolated in a 1.4-Th
573 window and accumulated to reach an AGC target value of 1e5 with a maximum injection time of 22
574 ms. Precursor ions with a charge state of 1 and 6 as well as isotopes were excluded for fragmentation.
575 Dynamic exclusion was set to 15s.

576 DDA raw files were processed with Proteome Discoverer (v. 2.2) using a human UniProt database
577 (release 201804) together with iRT peptides (Biognosys) and common contaminants. The processing
578 workflow consisted of SequestHT [42] and Amanda [43] nodes coupled with Percolator [44]. The following

579 search parameters were used for protein identification: (i) a peptide mass tolerance of 10 ppm; (ii) an
580 MS/MS mass tolerance of 0.02 Da; (iii) fully tryptic peptide search with up to two missed cleavages
581 were allowed; (iv) carbamidomethylation of cysteine was set as fixed modification, methionine
582 oxidation and protein N-term acetylation were set as variable modifications. Percolator was set at max
583 delta Cn 0.05, with target FDR strict 0.01 and target FDR relaxed 0.05. The spectral library from
584 Proteome Discoverer was imported into Spectronaut v12 (Biognosys, Schlieren, Switzerland) using
585 standard parameters with 0.01 peptide spectrum match (PSM) FDR.

586 DIA-MS setup and data analysis

587 For DIA analysis samples were measured on a Q Exactive HF mass spectrometer (Thermo Fisher
588 Scientific). Mobile phase A consisted of HPLC-grade water with 0.1% (v/v) formic acid, and mobile
589 phase B consisted of HPLC-grade ACN with 20% (v/v) HPLC-grade water and 0.1% (v/v) formic
590 acid. Peptide separation was carried out on an ES806, 2 µm, 100 Å, 150 µm i.d. x 150 mm, C18
591 EASY-Spray column (Thermo Fisher Scientific) at a temperature of 50°C. For LC-MS/MS analyses,
592 2 μg of each sample were loaded onto the column via an Easy-nLC 1200 system (Thermo Fisher
593 Scientific). Samples were loaded at 4 µL/min with 100% mobile phase A for 5 min. Peptide elution
594 was performed using the following gradient: i) 2% to 8% mobile phase B in 4 min, ii) 8% to 32%
595 mobile phase B in 49 min, iii) 32% to 60 % mobile phase B in 1 min, and iv) ramp to 98% mobile
596 phase B in 1 min at 2 µL/min.

597 For DIA-Acquisition on a Q Exactive HF mass spectrometer, we applied a DIA method published
598 elsewhere [45]. In short, we performed an MS1 scan over a mass range of m/z 400-1210 at a resolution
599 of 120,000 with an AGC target value of 3e6 and with a maximum injection time of 50 ms. For
600 MS/MS scans, resolution was at 0,000 with an AGC target value of 1e6 and with "Auto" maximum
601 injection time. Precursor ions were isolated within a 15-Th window and fragmented by HCD with
602 normalized collision energy 28. 54 MS/MS scan windows were defined, interspersed every 18 scans
603 with an MS1 scan.

604 DIA data Analysis was performed in Spectronaut v12 (Biognosys) using standard parameters. For
605 identification, a Qvalue cut-off of 0.01 was applied on the precursor as well as on the protein level.
606 The MS1 area was selected for quantification. Quantification parameters were set to mean peptide
607 quantity for major group quantity, the top 3 peptides were selected for protein quantity calculation.
608 Data filtering was set to Qvalue sparse, with no imputation. Cross-run normalization was set to local.
609 The protein report for downstream analysis contained information report about PG.ProteinAccessions,
610 PG.ProteinDescriptions, PG.ProteinNames. PG.Qvalue and PG.Quantity.

611 Selection of primary fibroblasts for polar metabolomics

612 To select cell lines for metabolomics, we opted for a balanced design with 10 MMUT deficient cell
613 lines and 10 control lines. MMUT deficient lines were picked to show over-expression of GLUD1 and
614 under-expression of OGDH whereas the control lines were chosen to show the reverse pattern. We
615 fitted a mixed effects model with PI+ as response, two fixed effects for GLUD1 and OGDH
616 expression, and a random effect with the same covariance structure as the proteomics data after
617 column and row normalization. From the MMUT deficient and control cell lines, we chose 10 with
618 the lowest predicted value of PI+ and 10 with the highest predicted value respectively. The top ten
619 ranked MMUT deficient (MMA014, MMA92, MMA042, MMA67, MMA93, MMA104, MMA013,
620 MMA030, MMA138, MMA036) and the last 10 ranked control primary fibroblasts (MMA219,
621 MMA221, MMA227, MMA222, MMA213, MMA230, MMA226, MMA228, MMA225, MMA215)
622 were selected and cultured as described above. Four primary fibroblasts in each group did not meet
623 growth criteria, most likely due to the long freezing period, and were excluded (MMA014, MMA92,
624 MMA042, MMA013, MMA219, MMA221, MMA227, MMA226). Six primary fibroblast lines per
625 group were selected for the polar metabolomics experiment.

626 Quality assessment of WGS, RNA-seq and DIA-MS data

627 Overall quality assurance tests revealed a mean of high-quality aligned genomic reads of 8.7×10^{8} at a
628 median genomic coverage of >38-fold (**Extended data Fig. 1b**). A median of 3.74 million SNVs

629 were called using the Genome Analysis Toolkit [46] and DeepVariant [47]. RNA-seq data showed a
630 median Phred score of >36.3 at three and more cycles (**Extended data Fig. 1c**), while proteomics data
631 showed a high reproducibility with 2218 proteins detected in at least 75% of samples (**Extended data**
632 **Fig. 1d**). For nine of the 230 samples RNA extraction yielded insufficient nucleic acid amounts to
633 proceed with transcriptome sequencing; hence, these datasets were excluded from all further analysis
634 (transcriptomics data of sample IDs 22, 54, 59, 78, 89, 109, 123, 207, 221).

635 Fibroblast sample preparation for polar metabolomics

636 100,000 cells per well were seeded in a 6 well plate and grown for 48 hours. Media was removed and
637 cells washed with 2 mL per well of 150 mM ammonium hydrogen carbonate (NH_4HCO_3) at pH 7.4
638 twice. The whole plate was flash-frozen in liquid nitrogen for 20 seconds and then stored at -80°C.
639 Metabolites were extracted by putting the plate on dry ice and adding 400 ul of cold (-20°C) 40:40:20
640 acetonitrile:methanol:water and incubated at -20°C for 10 minutes. Supernatant was collected. Added
641 another 400 ul of 40:40:20 acetonitrile:methanol:water and incubated at -20°C for 10 minutes. Plates
642 were put on dry ice and cells were scraped mechanically. The supernatant including the scraped cells
643 were collected in the same tube as during the first extraction step. Collection tubes were centrifuged at
644 13,000 rpm for 2 minutes at 4°C. Supernatants were stored at -20°C prior to metabolomics analysis.

645 Polar metabolomics in patient-derived fibroblasts

646 Untargeted metabolite profiling was performed using flow injection analysis on an Agilent 6550
647 QTOF instrument (Agilent, Santa Clara, CA) using negative ionization, 4 GHz high resolution
648 acquisition, and scanning in MS1 mode between m/z 50-1000 at 1.4 Hz [48]. The solvent was 60:40
649 isopropanol:water supplemented with 1 mM NH4F at pH 9.0, as well as 10 nM hexakis(1H, 1H, 3H-
650 tetrafluoropropoxy)phosphazine and 80 nM taurochloric acid for online mass calibration. The seven
651 batches were analyzed sequentially. Within each batch, the injection sequence was randomized. Data
652 was acquired in profile mode, centroided and analyzed with Matlab (The Mathworks, Natick).
653 Missing values were filled by recursion in the raw data. Upon identification of consensus centroids

654 across all samples, ions were putatively annotated by accurate mass and isotopic patterns. Starting
655 from the HMDB v4.0 database, we generated a list of expected ions including deprotonated,
656 fluorinated, and all major adducts found under these conditions. All formulas matching the measured
657 mass within a mass tolerance of 0.001 Da were enumerated. As this method does not employ
658 chromatographic separation or in-depth MS2 characterization, it is not possible to distinguish between
659 compounds with identical molecular formula. The confidence of annotation reflects Level 4 but – in
660 practice – in the case of intermediates of primary metabolism it is higher because they are the most
661 abundant metabolites in cells. The resulting data matrix included 1809 ions that could be matched to
662 deprotonated metabolites listed in HMDB. All m/z peaks that remained unmatched or were associated
663 to adducts or heavy isotopomers were discarded.

664 Mouse care and handling

665 Ethics approval was obtained prior to the study from the Cantonal Veterinary Office Zurich under the
666 license number 202/2014. Mice were kept under standard conditions, i.e. single-ventilated cages with
667 controlled humidity and room temperature of 22°C. Generation of the *Mmut*-p.Met698Lys variant
668 model and crossing with a *Mmut*-ko/wt model was done as previously described [23].

669 Harvesting of mouse tissues

670 Urine was collected in the morning after one night in a metabolic cage. The sediment was removed,
671 and supernatant was flash frozen in liquid nitrogen. Tissue samples were harvested from mice aged 58
672 to 63 days. Animals were anesthetized by sevoflurane. Portal blood was taken and kept on ice to
673 coagulate, centrifuged at 4°C and snap frozen in liquid nitrogen directly after. Liver, kidneys, heart,
674 and brain were harvested and snap-frozen in liquid nitrogen. After the procedure, the mice were
675 directly euthanized by cervical dislocation. All samples were stored at -80°C prior to analysis.

676 ## Metabolomics in mouse tissues

677 The mouse body fluid and tissue samples derived from five *Mmut*-ki/wt and five *Mmut*-ko/ki mice
678 were harvested as described above and prepared as previously published [49]. Sample analysis using
679 liquid chromatography-mass spectrometry was performed as previously published [50]. Ions were
680 annotated to metabolites based on exact mass to the KEGG database [51] considering [M-H+] and 0.01
681 Da mass accuracy. Significantly changing ions between mutant and control conditions were identified
682 using a two-sample t-test. Pathway analysis was performed using annotated ion list ranked by p-value
683 significance. Pathway enrichments were calculated using KEGG metabolic pathway definitions and a
684 hypergeometric test.

685 ## Transcriptomics in mouse brains

686 Brain tissue samples were harvested as described above. Four mice per genotype groups *Mmut*-ki/wt
687 and *Mmut*-ko/ki were used. RNA was purified using DNAse kit (Qiagen, No. 79254) together with
688 QIAmp RNA Blood Mini Kit (Qiagen, No. 52304). RNA-seq reads were aligned with the STAR-
689 aligner [52]. As reference we used the Ensembl mouse genome build GRCm38. Gene expression values
690 were computed with the function featureCounts from the R package Rsubread [53].

691 ## CRISPR gene-editing experiments

692 CRISPR-Cas9 editing was performed as described [54]. Cas9 protein was provided as a plasmid
693 (PX459-V2.0, Addgene, 62988) and guide RNA as gBLOCKS [55] (IDT Technologies). 293T cells
694 were transfected using the Neon transfection system (Thermo Fisher Scientific) containing 100,000
695 cells, 0.6 µg of Cas9 plasmid and 600 ng of guide RNA following manufacturer's instructions. 48 h
696 after transfection, cells were collected, diluted to 1 cell/100 µl and transferred to a 96-well plate at 100
697 µl/well for clonal selection. Correct clones were confirmed by Sanger sequencing of genomic DNA.

698 ## Western blotting

699 Lysates of 293T cell lines were mixed with RIPA lysis buffer and 4X Laemmli buffer to obtain a
700 concentration of 1 µg/µl protein. Samples were incubated at 96°C for 5 minutes. 20 µl of each sample
701 was loaded onto a 10% SDS page gel. Proteins were separated by electrophoresis, transferred with a
702 semi-dry method onto a nitrocellulose membrane (Whatman, GE Healthcare), blocked at room
703 temperature for 2 hours with buffer A (5% skimmed milk, 1.2% w/v Tris-base, 9% w/v NaCl, 0.2%
704 Tween 20, pH 7.6), incubated with primary antibodies dissolved in buffer A overnight at 4°C, and
705 detected using secondary antibodies in buffer A. Primary antibodies used were probing for the
706 following proteins: MMUT (Abcam, ab67869, 1:1000, host: mouse), OGDH (Atlas antibodies,
707 HPA020347, 1:500, host: rabbit), GLUD (Abcam, ab166618, 1:2000, host: rabbit), Beta-actin (Sigma,
708 A1978, 1:5000, host: mouse). Secondary antibodies used were Anti-rabbit HRP (Santa Cruz, sc-2357,
709 1:5000, host: mouse), Anti-mouse HRP (Santa Cruz, sc-516102, 1:5000, host: goat).

710 ## MMUT enzyme activity assay

711 Confluent cells from a T75 were detached using trypsin, the cell suspension centrifuged at 250 *g*, the
712 pellet washed two-times 1 mL in PBS and the supernatant discarded. Homogenates were obtained by
713 resuspension of cell pellets in 150 µL of 5 mM KH_2PO_4 (pH 7.4) followed by sonication on ice with 2
714 pulses for 15 seconds using the microprobe of an XL-2000 (Microson, Qsonica, Newtown, CT, USA)
715 with amplitude set to 2 microns. The homogenate was then diluted 1:4 in a final concentration of 50
716 µM adenosylcobalamin (Sigma C0884), 1 mM methylmalonyl-CoA (Sigma M1762) and 0.1 M assay
717 buffer KH_2PO_4. The enzymatic reaction was performed at 37°C for 30 min. Subsequently, the reaction
718 was stopped, and succinyl-CoA hydrolysed by addition of 500 mM KOH and incubation at 37°C for
719 15 min. The assay mixture was neutralized with $HClO_4$ at a final concentration of 400 mM, the
720 sample centrifuged at 16,000 *g* and the supernatant discarded. Precipitates were frozen at -20 degrees
721 until further analysis. For mass spectrometry, the MMUT-KO sample was diluted 1:2, the WT sample
722 was diluted 1:50 in a dilution solution (Recipe, MS5021) and then precipitated with 4 parts
723 precipitation reagent with internal standard (Recipe, MS5112). After centrifugation (5min, 16’000 *g*)

724 the supernatant was transferred into a fresh vial. Final succinate determination was performed by
725 HPLC separation and electrospray tandem mass spectrometry (ESI-MS/MS) detection (SCIEX
726 TripleQuad 5500 LC-MS/MS System).

727 KGDH enzyme activity assays

728 Assay of oxoglutarate dehydrogenase enzyme activity was performed in 293T cell clones according to
729 the manufacturer's instructions (Sigma-Aldrich, St. Louis, USA, catalogue number MAK189) using
730 the plate reader Victor Nivo by PerkinElmer.

731 Glutamine tracing studies

732 293T cells were cultured on coverslips in DMEM (Gibco, catalog number: 11960044) without L-
733 glutamine, sodium pyruvate and HEPES supplemented with 10% FBS, 1% antibiotic-antimycotic
734 (Gibco), and [U-^{13}C]glutamine (final concentration 4 mM) (Sigma-Aldrich, catalog number: 605166)
735 for 4 hours. Medium was then removed, coverslips were quickly dipped into sterile double-distilled
736 water at 37°C and quenched in 80% methanol at -80°C. Cells were scrapped in methanol, collected,
737 and centrifuged at 15'000 g for 15 minutes at 4°C. Supernatants were collected, snap frozen in liquid
738 nitrogen, and stored at -80°C prior to LC/MS analysis.

739 300 µl of sample was lyophilized overnight until dry and resolubilized in 200 µl loading buffer
740 (water, 0.5% formic acid) in narrow-bottom 96-deep well plates on shaker (800 rpm, 15°C, 10 min)
741 for LC-MS injection. Metabolites were separated using a ACQUITY UPLC HSS T3 1.8 µm, 100 x
742 2.1 mm I.D. column (Waters, Massachusetts, US) and eluted using the following gradient from
743 solvent A (water, 5 mM ammonium formate, 0.1% formic acid) to solvent B (methanol, 5 mM
744 ammonium formate, 0.1% formic acid) as follows: 2 minutes at 0% B, 2-3.5 mins to 4% B, 3.5-10
745 mins to 45% B, 10-12 mins to 70% B, 12-13.5s min to 100% B, with a isocratic plateau at 100% B for
746 2 mins to 15.5 mins, and from 15.5-16.5 mins to 0%B. After each run the column was re-equilibrated
747 for 8 mins at 100% A with a constant flow rate of 0.4ml/min.

748 Mass spectra were acquired using a heated electro-spray ionization (HESI) source of a Q-Exactive
749 high resolution, accurate mass spectrometer (Thermo Scientific, Waltham, MS, USA). Mass spectra
750 were recorded in positive and negative mode with the MS detector in full-scan mode (Full-MS) in the
751 scan-range 50 to 750 m/z with an automatic gain control target of 1e6, an Orbitrap resolution of
752 70,000, and a maximum injection time of 80 ms. Peaks were integrated with Xcalibur (version
753 4.0.27.19, Thermo Fisher Scientific) using windows of 0.01 m/z and 20 seconds for retention time as
754 previously determined using a library of standards.

755 HESI parameters: sheath gas flow rate 35 arbitrary units (AU), auxiliary gas flow rate 35 AU, sweep
756 gas flow rate 2 AU, spray voltage 3.5 kV, capillary temperature 350°C, aux gas heater temperature
757 350°C. Detector settings for full MS: In-source CID 0.0 eV, µscans = 1, resolution = 70,000, AGC
758 target 1e6, max IT = 35 ms, spectrum data type, profile. Integration parameters: ICIS Peak
759 Integration, nearest RT, smoothing points 3, baseline window 40, area noise factor 3, peak noise
760 factor 70, minimum peak height 3.0.

761 Data preprocessing included missing value imputation and normalization to internal standards $[^2H]_3$-
762 creatine and $[^2H]_4$-citric acid for positive and negative mode respectively.

763 Affinity capture mass spectrometry

764 293T cells (ATCC #CRL-3216; Manassas, WV) were grown in Dulbecco's Modified Eagle Medium
765 (Gibco, Carlsbad, CA) supplemented with 10% fetal bovine serum (Gibco) and antibiotics (GE
766 Healthcare). Transient transfection of pCDNA3-C-Flag-LIC constructs was performed using
767 Lipofectamine 3000 (Thermo Fisher Scientific) according to manufacturer's instructions. 48 h after
768 transfection, cells were crosslinked using 0.5% paraformaldehyde (PFA, Sigma-Aldrich) in PBS
769 (Gibco) for 10 min at RT, the reaction was quenched with 1.25 M glycine/PBS (Sigma-Aldrich) for
770 10 min at 4°C, cells were centrifuged for 5 min at 2,000×*g* at 4°C, and the pellet resuspended in lysis
771 buffer (1% Nonidet P-40, 0.5% deoxycholine, 150 mM NaCl, 50 mM Tris–HCl, pH7.5, all Sigma-
772 Aldrich). Pre-cleared cell extracts were immunoprecipitated with anti-flag M2 (F3165, Sigma–
773 Aldrich) using Dynabeads Protein G (Thermo Fisher Scientific) according to the manufacturer's

774 instructions. Following washing, peptides were released by trypsin (100 ng/µl in 10 mM HCl) and
775 supernatants collected, dried, dissolved in 0.1% formic acid.

776 All affinity-captured samples were measured on a Q Exactive mass spectrometer (Thermo Fisher
777 Scientific) with a MS1 resolution of 70,000 and an AGC target of 3e6 and a maximum injection time
778 of 100 ms over a scan range of m/z 350-1500. A data-dependent top 12 method was used for HCD
779 MS/MS with a normalized collision energy of 25 at a resolution of 35,000. Precursor ions were
780 isolated in a 1.2-Th window with an AGC target value of 1e5 with a maximum injection time of 120
781 ms. Dynamic exclusion was set to 40s.

782 Samples were analyzed using Mascot (Matrix Science, London, UK; version 2.6.2) with the SwissProt
783 database (download date 20190204) assuming trypsin with at maximum two miscleavages. Mascot
784 was searched with a fragment ion mass tolerance of 0.030 Da and a parent ion tolerance of 10.0 PPM.
785 Oxidation of methionine was specified as a variable modification. Scaffold (version Scaffold_5.1.2,
786 Proteome Software Inc., Portland, OR) was used to validate MS/MS based peptide and protein
787 identifications. Peptide identifications were accepted if they could be established at greater than
788 95.0% probability by the Scaffold Local FDR algorithm. Protein identifications were accepted if they
789 could be established at greater than 99.0% probability and contained at least 2 identified peptides.

790 Data analysis

791 Data analysis was performed using R version 4.1.0. For the global data layer inspection we used the
792 MOFA package version 1.3.1 [22], the MASS package version 7.3-54 [56], the fgsea package version
793 1.18.0 [57]. Gene enrichment analysis was performed using gene sets downloaded from
794 http://www.gsea-msigdb.org/gsea/msigdb/index.jsp "MSigDB Collections" on 28 December 2020.
795 Circos including chord plots were created using the circlize package version 0.4.13 [58]. The Uniprot
796 portal was accessed on 24 February 2021 at 4 PM to scrape protein localization data. The code for all
797 the analyses and generation of figures is hosted on a repository on the GitHub platform under
798 https://github.com/pforny/MMAomics.

Genetic variant investigation approach

Short variant calling was carried out with GATK and Deep Variant algorithms, and annotated with annovar [59]. CNVs were called with CNVnator [60] with a bin size of 100 and standard parameters, and annotated with AnnotSV [61]. Variation in the *MMUT* gene was investigated first. When no genetic cause for the phenotype was identified with this approach (two inactivating/damaging events in *MMUT*), other genes known to be involved in MMA (based on literature reports) were investigated as a virtual gene panel. When no genetic cause was found in the two previous steps, genes highlighted by mutational burden (genes harboring pathogenic variants across the cohort in an autosomal recessive pattern in two or more individuals) were investigated. Finally, all samples and controls were used to run OUTRIDER [19], and genes highlighted as expression outliers associated with phenotypes overlapping MMA were analyzed to either confirm the identified damaging variants, or to further explore damaging variation in them.

Variants were prioritized with the following approach: First, any coding variant (excluding synonymous variants) with a GnomAD frequency across all represented populations <0.01, in homozygosity or compound heterozygosity with another relevant variant, and supported by at least two forward and two reverse reads and at least 8 reads coverage, were evaluated. Second, all variants categorized by the automatic application of the ACMG criteria [62] by InterVar [63], or classified in ClinVar [64] as “pathogenic” or “likely pathogenic”, in homozygosity or compound heterozygosity with another relevant variant, were considered and evaluated. Third, variants with a dbscSNV_ADA or dbscSNV_RF scores >0.6 in the annovar annotation using the database prepared and described previously [65] were evaluated.

For CNVs, individuals with a single heterozygous variant or no variation in *MMUT* and the other genes of interest were investigated for the presence of relevant CNVs that could explain their phenotype [59].

824 # References

825 1. Argmann, C. A., Houten, S. M., Zhu, J. & Schadt, E. E. A Next Generation Multiscale View of
826 Inborn Errors of Metabolism. *Cell Metab* **23**, 13–26 (2016).
827 2. Garrod, ArchibaldE. The Croonian Lectures ON INBORN ERRORS OF METABOLISM. *The*
828 *Lancet* **172**, 1–7 (1908).
829 3. Ferreira, C. R., Rahman, S., Keller, M. & Zschocke, J. An international classification of inherited
830 metabolic disorders (ICIMD). *Journal of Inherited Metabolic Disease* **44**, 164–177 (2021).
831 4. Rahman, S. Mitochondrial disease in children. *J Intern Med* **287**, 609–633 (2020).
832 5. Hirano, M., Emmanuele, V. & Quinzii, C. M. Emerging therapies for mitochondrial diseases.
833 *Essays Biochem* **62**, 467–481 (2018).
834 6. 100,000 Genomes Project Pilot Investigators *et al.* 100,000 Genomes Pilot on Rare-Disease
835 Diagnosis in Health Care - Preliminary Report. *N Engl J Med* **385**, 1868–1880 (2021).
836 7. Palmer, E. E. *et al.* Diagnostic Yield of Whole Genome Sequencing After Nondiagnostic Exome
837 Sequencing or Gene Panel in Developmental and Epileptic Encephalopathies. *Neurology* **96**,
838 e1770–e1782 (2021).
839 8. Schon, K. R. *et al.* Use of whole genome sequencing to determine genetic basis of suspected
840 mitochondrial disorders: cohort study. *BMJ* e066288 (2021) doi:10.1136/bmj-2021-066288.
841 9. Cummings, B. B. *et al.* Improving genetic diagnosis in Mendelian disease with transcriptome
842 sequencing. *Sci Transl Med* **9**, eaal5209 (2017).
843 10. Kremer, L. S. *et al.* Genetic diagnosis of Mendelian disorders via RNA sequencing. *Nat Commun*
844 **8**, 15824 (2017).
845 11. Gonorazky, H. D. *et al.* Expanding the Boundaries of RNA Sequencing as a Diagnostic Tool for
846 Rare Mendelian Disease. *Am J Hum Genet* **104**, 466–483 (2019).
847 12. Frésard, L. *et al.* Identification of rare-disease genes using blood transcriptome sequencing and
848 large control cohorts. *Nat Med* **25**, 911–919 (2019).
849 13. Froese, D. S. & Gravel, R. A. Genetic disorders of vitamin B_{12} metabolism: eight
850 complementation groups--eight genes. *Expert Rev Mol Med* **12**, e37 (2010).

851 14. Forny, P., Froese, D. S., Suormala, T., Yue, W. W. & Baumgartner, M. R. Functional
852 characterization and categorization of missense mutations that cause methylmalonyl-CoA mutase
853 (MUT) deficiency. *Hum Mutat* **35**, 1449–1458 (2014).
854 15. Froese, D. S. *et al.* Structures of the Human GTPase MMAA and Vitamin B12-dependent
855 Methylmalonyl-CoA Mutase and Insight into Their Complex Formation*,. *Journal of Biological*
856 *Chemistry* **285**, 38204–38213 (2010).
857 16. Ruetz, M. *et al.* Itaconyl-CoA forms a stable biradical in methylmalonyl-CoA mutase and derails
858 its activity and repair. *Science* **366**, 589–593 (2019).
859 17. Jost, M., Cracan, V., Hubbard, P. A., Banerjee, R. & Drennan, C. L. Visualization of a radical
860 B12 enzyme with its G-protein chaperone. *Proc Natl Acad Sci U S A* **112**, 2419–2424 (2015).
861 18. Froese, S. & Baumgartner, M. R. Lysosomal Vitamin B12 Trafficking. in *Ion and Molecule*
862 *Transport in Lysosomes* (CRC Press, 2020).
863 19. Brechtmann, F. *et al.* OUTRIDER: A Statistical Method for Detecting Aberrantly Expressed
864 Genes in RNA Sequencing Data. *The American Journal of Human Genetics* **103**, 907–917
865 (2018).
866 20. Forny, P. *et al.* Guidelines for the diagnosis and management of methylmalonic acidaemia and
867 propionic acidaemia: First revision. *Journal of Inherited Metabolic Disease* **44**, 566–592 (2021).
868 21. Hörster, F. *et al.* Prediction of outcome in isolated methylmalonic acidurias: combined use of
869 clinical and biochemical parameters. *Journal of Inherited Metabolic Disease* **32**, 630 (2009).
870 22. Argelaguet, R. *et al.* Multi-Omics Factor Analysis-a framework for unsupervised integration of
871 multi-omics data sets. *Mol Syst Biol* **14**, e8124 (2018).
872 23. Forny, P. *et al.* Novel Mouse Models of Methylmalonic Aciduria Recapitulate Phenotypic Traits
873 with a Genetic Dosage Effect. *J Biol Chem* **291**, 20563–20573 (2016).
874 24. Lamparter, D., Marbach, D., Rueedi, R., Bergmann, S. & Kutalik, Z. Genome-Wide Association
875 between Transcription Factor Expression and Chromatin Accessibility Reveals Regulators of
876 Chromatin Accessibility. *PLOS Computational Biology* **13**, e1005311 (2017).
877 25. Rath, S. *et al.* MitoCarta3.0: an updated mitochondrial proteome now with sub-organelle
878 localization and pathway annotations. *Nucleic Acids Res* **49**, D1541–D1547 (2021).

879 26. Nusinow, D. P. *et al.* Quantitative Proteomics of the Cancer Cell Line Encyclopedia. *Cell* **180**,
880 387-402.e16 (2020).
881 27. Williams, E. G. *et al.* Systems proteomics of liver mitochondria function. *Science* **352**, aad0189–
882 aad0189 (2016).
883 28. Heusel, M. *et al.* Complex-centric proteome profiling by SEC-SWATH-MS. *Mol Syst Biol* **15**,
884 e8438 (2019).
885 29. Buescher, J. M. *et al.* A roadmap for interpreting (13)C metabolite labeling patterns from cells.
886 *Curr Opin Biotechnol* **34**, 189–201 (2015).
887 30. Chen, Q. *et al.* Rewiring of Glutamine Metabolism Is a Bioenergetic Adaptation of Human Cells
888 with Mitochondrial DNA Mutations. *Cell Metabolism* **27**, 1007-1025.e5 (2018).
889 31. Zhang, J. *et al.* 13C isotope-assisted methods for quantifying glutamine metabolism in cancer
890 cells. *Methods Enzymol* **542**, 369–389 (2014).
891 32. Liu, A. *et al.* From expression footprints to causal pathways: contextualizing large signaling
892 networks with CARNIVAL. *npj Syst Biol Appl* **5**, 1–10 (2019).
893 33. Lewis, J. E., Forshaw, T. E., Boothman, D. A., Furdui, C. M. & Kemp, M. L. Personalized
894 Genome-Scale Metabolic Models Identify Targets of Redox Metabolism in Radiation-Resistant
895 Tumors. *Cell Systems* **12**, 68-81.e11 (2021).
896 34. Wang, H. *et al.* Genome-scale metabolic network reconstruction of model animals as a platform
897 for translational research. *PNAS* **118**, (2021).
898 35. Sloan, J. L. *et al.* Exome sequencing identifies ACSF3 as a cause of combined malonic and
899 methylmalonic aciduria. *Nat Genet* **43**, 883–886 (2011).
900 36. Karczewski, K. J. & Snyder, M. P. Integrative omics for health and disease. *Nat Rev Genet* **19**,
901 299–310 (2018).
902 37. Vockley, J. *et al.* Effects of triheptanoin (UX007) in patients with long-chain fatty acid oxidation
903 disorders: Results from an open-label, long-term extension study. *J Inherit Metab Dis* **44**, 253–
904 263 (2021).
905 38. Longo, N. *et al.* Anaplerotic therapy in propionic acidemia. *Mol Genet Metab* **122**, 51–59 (2017).

906 39. Willard, H. F., Ambani, L. M., Hart, A. C., Mahoney, M. J. & Rosenberg, L. E. Rapid prenatal
907 and postnatal detection of inborn errors of propionate, methylmalonate, and cobalamin
908 metabolism: a sensitive assay using cultured cells. *Hum Genet* **34**, 277–283 (1976).
909 40. Baumgartner, R. Activity of the cobalamin-dependent methylmalonyl-CoA mutase. *The*
910 *Cobalamins: Methods in Hematology. Churchill Livingstone, Edinburgh, New York* 181–195
911 (1983).
912 41. Causey, A. G. & Bartlett, K. A radio-HPLC assay for the measurement of methylmalonyl-CoA
913 mutase. *Clinica Chimica Acta* **139**, 179–186 (1984).
914 42. Eng, J. K., McCormack, A. L. & Yates, J. R. An approach to correlate tandem mass spectral data
915 of peptides with amino acid sequences in a protein database. *J Am Soc Mass Spectrom* **5**, 976–989
916 (1994).
917 43. Dorfer, V. *et al.* MS Amanda, a universal identification algorithm optimized for high accuracy
918 tandem mass spectra. *J Proteome Res* **13**, 3679–3684 (2014).
919 44. Brosch, M., Yu, L., Hubbard, T. & Choudhary, J. Accurate and sensitive peptide identification
920 with Mascot Percolator. *J Proteome Res* **8**, 3176–3181 (2009).
921 45. Xuan, Y. *et al.* Standardization and harmonization of distributed multi-center proteotype analysis
922 supporting precision medicine studies. *Nat Commun* **11**, 5248 (2020).
923 46. McKenna, A. *et al.* The Genome Analysis Toolkit: a MapReduce framework for analyzing next-
924 generation DNA sequencing data. *Genome Res* **20**, 1297–1303 (2010).
925 47. Poplin, R. *et al.* A universal SNP and small-indel variant caller using deep neural networks. *Nat*
926 *Biotechnol* **36**, 983–987 (2018).
927 48. Fuhrer, T., Heer, D., Begemann, B. & Zamboni, N. High-throughput, accurate mass metabolome
928 profiling of cellular extracts by flow injection-time-of-flight mass spectrometry. *Anal Chem* **83**,
929 7074–7080 (2011).
930 49. Want, E. J. *et al.* Global metabolic profiling of animal and human tissues via UPLC-MS. *Nat*
931 *Protoc* **8**, 17–32 (2013).
932 50. Abela, L. *et al.* Plasma metabolomics reveals a diagnostic metabolic fingerprint for mitochondrial
933 aconitase (ACO2) deficiency. *PLoS One* **12**, e0176363 (2017).

934 51. Kanehisa, M., Furumichi, M., Tanabe, M., Sato, Y. & Morishima, K. KEGG: new perspectives on
935 genomes, pathways, diseases and drugs. *Nucleic Acids Res* **45**, D353–D361 (2017).
936 52. Dobin, A. *et al.* STAR: ultrafast universal RNA-seq aligner. *Bioinformatics* **29**, 15–21 (2013).
937 53. Liao, Y., Smyth, G. K. & Shi, W. The Subread aligner: fast, accurate and scalable read mapping
938 by seed-and-vote. *Nucleic Acids Res* **41**, e108 (2013).
939 54. Ran, F. A. *et al.* Genome engineering using the CRISPR-Cas9 system. *Nat Protoc* **8**, 2281–2308
940 (2013).
941 55. Arbab, M., Srinivasan, S., Hashimoto, T., Geijsen, N. & Sherwood, R. I. Cloning-free CRISPR.
942 *Stem Cell Reports* **5**, 908–917 (2015).
943 56. Venables, W. N. & Ripley, B. D. *Modern applied statistics with S*. (Springer, 2002).
944 57. Korotkevich, G. *et al. Fast gene set enrichment analysis*. 060012
945 https://www.biorxiv.org/content/10.1101/060012v3 (2021) doi:10.1101/060012.
946 58. Gu, Z., Gu, L., Eils, R., Schlesner, M. & Brors, B. circlize Implements and enhances circular
947 visualization in R. *Bioinformatics* **30**, 2811–2812 (2014).
948 59. Wang, K., Li, M. & Hakonarson, H. ANNOVAR: functional annotation of genetic variants from
949 high-throughput sequencing data. *Nucleic Acids Res* **38**, e164 (2010).
950 60. Abyzov, A., Urban, A. E., Snyder, M. & Gerstein, M. CNVnator: an approach to discover,
951 genotype, and characterize typical and atypical CNVs from family and population genome
952 sequencing. *Genome Res* **21**, 974–984 (2011).
953 61. Geoffroy, V. *et al.* AnnotSV: an integrated tool for structural variations annotation.
954 *Bioinformatics* **34**, 3572–3574 (2018).
955 62. Richards, S. *et al.* Standards and guidelines for the interpretation of sequence variants: a joint
956 consensus recommendation of the American College of Medical Genetics and Genomics and the
957 Association for Molecular Pathology. *Genet Med* **17**, 405–424 (2015).
958 63. Li, Q. & Wang, K. InterVar: Clinical Interpretation of Genetic Variants by the 2015 ACMG-
959 AMP Guidelines. *Am J Hum Genet* **100**, 267–280 (2017).
960 64. Landrum, M. J. *et al.* ClinVar: improving access to variant interpretations and supporting
961 evidence. *Nucleic Acids Res* **46**, D1062–D1067 (2018).

962 65. Jian, X., Boerwinkle, E. & Liu, X. In silico prediction of splice-altering single nucleotide
963 variants in the human genome. *Nucleic Acids Res* **42**, 13534–13544 (2014).

964